Contents lists available at ScienceDirect

Journal of Energy Storage

journal homepage: www.elsevier.com/locate/est

Research papers

A sulfur host based on silicon oxycarbide for advanced lithium-sulfur batteries

Murilo M. Amaral [a,b], Shakir Bin Mujib [b], Erick A. Santos [a,c], Josimar Ribeiro [d], Hudson Zanin [a], Gurpreet Singh [b,*]

[a] Advanced Energy Storage Division, Center for Innovation on New Energies, University of Campinas, 13083-852 São Paulo, Brazil
[b] Mechanical and Nuclear Engineering Department, Kansas State University, Manhattan, KS 66506, USA
[c] Brazilian Center for Research in Energy and Materials (CNPEM)/Brazilian Synchrotron Light Laboratory (LNLS), Campinas, 13083-100 São Paulo, Brazil
[d] Laboratório de Pesquisa e Desenvolvimento em Eletroquímica (LPDE) - Department of Chemistry, Center of Exact Sciences, Federal University of Espírito Santo, Campus Goiabeiras, Av. Fernando Ferrari, Vitória 29075-910, Espírito Santo, Brazil

ARTICLE INFO

Keywords:
Silicon oxycarbide
Lithium-sulfur batteries
Porous structure
Shuttle effect

ABSTRACT

Lithium-sulfur (Li—S) batteries are promising battery systems that provide high capacity and energy density using abundant materials, but they have a significant drawback known as the shuttle effect, which restricts their capacity, increases their internal resistance, and results in poor cyclability. Therefore, several efforts are being focused on overcoming this drawback, including the development of novel cathode materials based on carbonaceous hosts to adsorb lithium polysulfides (LiPS) and inhibit the shuttle effect, which is a challenging task. In this context, this study investigates the use of silicon oxycarbide (SiOC) as the sulfur host for Li—S systems with outstanding electrochemical performance. SiOC powder has been synthesized by pyrolysis process at 800 °C, using 1,3,5-trivinyl-1,1,3,5,5-pentamethyltrisiloxane (TPTS) as the precursor. The sulfur loading procedure consists of a melt-diffusion process conducted at 150 °C, which successfully diffused sulfur into the SiOC porous structure. Then, the S-SiOC composite material morphology and structure have been investigated by several techniques, which confirmed the efficacy of the sulfur loading process. The S-SiOC composite cathode provides a stable capacity, presenting a reversible charge capacity of 711 mAh g_s^{-1} (≈ 50.3 % of its initial capacity) after 50 cycles at a current density of 83.75 mA g_s^{-1} (0.05C, considering 1C = 1675 mA g_s^{-1}), indicating that this composite is a promising material for Li—S batteries.

1. Introduction

The increasing demands for energy and renewable resources and the simultaneous need to decrease fossil fuel consumption necessitate the investigation of novel, high-performance energy storage systems. Although lithium-ion batteries (LIBs) have been widely employed in various fields, especially portable electronics, there is still a demand for novel battery systems with low-cost, high energy density, and high capacity. Among alternative systems, Li—S batteries are conversion batteries that use sulfur as the active cathode material, a material abundant on the earth's crust [1]. Li—S batteries have received significant attention due to their energy density of 2600 Wh kg^{-1} and sulfur's theoretical capacity of 1675 mAh g^{-1} [2]. Also, Li—S cells present an overall low cost, which is suitable for the fabrication of pouch cells, and further provide affordable commercial batteries [3].

The study of Li—S batteries started when sulfur was initially investigated as a cathode material by Herbert Danuta and Ulam Juliusz, and this electrochemical system was patented in 1962 [4]. However, the insulating nature of sulfur, the extreme volume change (≈ 80 %) during the conversion reactions, and the high solubility of LiPS in the electrolytes have hindered the practical realization of Li—S batteries [1]. These disadvantages have also created considerable challenges for the development of a reversible, efficient, and stable sulfur cathode [5]. However, one of the major contributions to overcoming these disadvantages of Li—S batteries was presented in 2009 by Ji, Lee, and Nazar, who introduced a carbon-sulfur composite cathode (70 wt% S), capable of adsorbing LiPS during redox reactions, reaching capacity values up to 1320 mAh g^{-1}, which was approximately three times higher than the capacity of traditional LIBs [6].

After the study presented by Ji, Lee, and Nazar [6], several

* Corresponding author.
E-mail address: gurpreet@ksu.edu (G. Singh).

https://doi.org/10.1016/j.est.2023.108388
Received 20 April 2023; Received in revised form 6 July 2023; Accepted 13 July 2023

carbonaceous materials have been investigated as the sulfur host of Li—S batteries' cathode in order to identify materials that can efficiently adsorb LiPS dissolved in the electrolyte, and provide high capacity retention, such as carbon nanotubes [7], graphene [8], reduced graphene oxide [9], activated carbon [10], and carbon nanofibers [11]. However, in many cases involving carbon-host material, the sulfur cathode suffered capacity degradation or low energy density due to weak physical adsorption of LiPS in the carbon host [1]. Therefore, to overcome this challenge and reduce the shuttle effect, polar compounds such as metal oxides nanoparticles [12], metal sulfides [13], and metal-organic frameworks [14], including a recent study involving vapor silica [15], have been proposed as alternative hosts for sulfur cathode because the strong chemical adsorption capability of these polar compounds helps to immobilize LiPS. Nonetheless, there is a need to design materials that can efficiently adsorb LiPS, which requires the investigation of new materials with high specific surface area (SSA) and porosity, aiming to inhibit the shuttle effect and provide a long cyclability [16].

Silicon (Si)-based polymer-derived ceramics (PDCs), such as SiOC, are achieved by thermal degradation of polymer precursors comprised of polar silica domains that offer adsorption sites for LiPS and a free-carbon domain network that improves the electrical conductivity of the SiOC. Consequently, PDCs have an appropriate matrix for hosting sulfur once they present a porous amorphous structure, high conductivity, and resistance against high temperature and corrosion [17,18]. PDCs have also been extensively studied as an anode material for LIBs, particularly SiOC, which has shown electrochemical capacity significantly higher than the capacity of a conventional graphite electrode, and has been studied using different polymer precursors and composites [19,20]. However, PDCs have been rarely investigated as the sulfur hosts for the cathodes of Li—S batteries; and the recent investigations of SiCN [21,22] and SiOCN [23] have demonstrated high electrochemical stability due to the confinement of LiPS via physical and chemical adsorption through Li—N bonds and polar silica domains of the PDC materials. In addition, Weinberger et al. [24] investigated carbon derived from SiOC (SiOCDC) as a sulfur host for Li—S batteries, which demonstrated a reversible capacity of 241 mAh g^{-1} after 100 cycles. Thus, other PDC compositions derived from low-cost and readily available polysiloxanes that yield $Si_xO_yC_z$ or C-rich SiOC upon pyrolysis may be equally or more effective sulfur-hosts, given the similarities with SiCN in the microstructure. However, these compositions have still not been studied.

A previous study conducted by Mujib et al. [25] investigated the performance of $Si_xO_yC_z$ fibers obtained from three distinct polymer precursors: 1,5-divinyl-3,3-diphenyl-1,1,5,5-tetramethyltrisiloxane (DDTS); 1,3-divinyltetramethyldisiloxane (DTDS); and TPTS. Results showed that the hollow structure of TPTS-derived SiOC material was advantageous due to the high SSA and high free-carbon content of TPTS-SiOC [25]. These results prompted the current investigation of the use of TPTS-SiOC as a conducting sulfur host for Li—S batteries.

Herein, this research article presents the first report on the application of SiOC powder derived from TPTS precursor, as the sulfur host for a Li—S battery that was pyrolyzed at 800 °C. The SiOC ceramic powder has efficiently loaded sulfur in its structure, presenting stable electrochemical performance and inhibiting the shuttle effect. Electrochemical tests were performed to study the Li—S battery with the S-SiOC cathode, and the S-SiOC electrode was characterized by ex-situ and post-cycling morphological and structural analysis. The S-SiOC cathode presented a reversible charge capacity of 711 mAh g_s^{-1} (≈ 50.3 % of its initial capacity) after 50 cycles at a current density of 83.75 mA g_s^{-1} (i.e., 0.05C, considering 1C = 1675 mA g_s^{-1}), which is a significant capacity retention once the system presented a stable result, and most of the capacity loss was observed in the initial cycles. Furthermore, the S-SiOC cathode provided significant capacity retention for the current density of 167.5 mA g_s^{-1} (0.1C, considering 1C = 1675 mA g_s^{-1}), and presented a reversible capacity of 398 mAh g_s^{-1} (≈ 34.25 % of its initial capacity) after 300 cycles and 203 mAh g_s^{-1} (≈ 17.47 % of its initial capacity) after 500 cycles.

2. Materials and methods

2.1. Electrode fabrication

This study used TPTS, purchased from Gelest, Inc. (Pennsylvania, USA), as the precursor of the SiOC ceramic. The precursor was mixed with 1 wt% dicumyl peroxide (DCP), purchased from Sigma-Aldrich (Missouri, USA). The cross-linking process was conducted at 160 °C for 12 h inside a glove box filled with ultrahigh purity (99.99 %) argon (Ar) supplied by Matheson (Kansas, USA). The powder was then pyrolyzed in an alumina tube furnace under Ar flow at 800 °C for 30 min, with a heating rate of 2 °C/min, resulting in the SiOC powder. To create a sulfur-SiOC (S-SiOC) composite, 70 wt% sulfur (S_8) powder (Sigma-Aldrich) was mixed with 30 wt% SiOC inside a Teflon vessel (inlet) and positioned inside an autoclave that was heated at 150 °C for ≈ 16 h to enable the melt-diffusion process. Next, the powders were removed from the Teflon vessel and ground using a mortar pestle until they became a homogeneous powder, resulting in an S-SiOC composite (the process is summarized in Fig. 1).

2.2. Li—S cell preparation

The S-SiOC composite electrode was prepared from a slurry containing 80 wt% S-SiOC composite powder (S:SiOC, 70:30 wt. %), 10 wt% carbon black (Alfa Aesar, Massachusetts, USA) as the conducting agent, and 10 wt% polyvinylidene fluoride (PVDF) (Sigma-Aldrich) as a binder. S-SiOC powder, carbon black, and PVDF were ground for 30 min using a mortar pestle, and then drops of *N*-methyl 2 pyrrolidone (NMP) (Alfa Aesar) were added to form a slurry (i.e., S-SiOC). The slurry was coated over an aluminum foil via a doctor blading method, and heated at 80 °C overnight.

After the drying process, discs with a diameter of 9/16″ (14.2875 mm) were punched out of the aluminum foil and used as the cathodes of the Li—S cells. The S-SiOC composite electrodes presented an average sulfur loading of ≈ 0.65–0.7 $mg_s\ cm^{-2}$. Although some studies presented in the literature have reported cathodes for Li—S batteries with sulfur loading higher than 4 $mg_s\ cm^{-2}$, aiming to achieve the highest possible energy density [26,27], other studies have investigated the fundamentals of novel sulfur hosts by using electrodes with lower values of sulfur loading (i.e., lower than 2 $mg_s\ cm^{-2}$) [23,28,29]. The main focus of this work was to understand the electrochemical behavior of SiOC as a sulfur host in the S-SiOC composite as a cathode for Li—S batteries.

To prepare the electrolyte, 1 M LiTFSI (Sigma-Aldrich) was dissolved into 1,3-dioxolane (DOL) (Sigma-Aldrich) and 1,2-dimethoxyethane (DME) (Sigma-Aldrich) (v/v, 1:1), with 1 wt% $LiNO_3$ (Sigma-Aldrich) as the additive, which is an efficient electrolyte composition for forming the passivation layer over the lithium metal anode, providing electrochemical stability to Li—S batteries, and controlling the shuttle effect [30,31]. The separator used was a glass fiber membrane with a diameter of approximately 19 mm and a thickness of 25 μm (GE, USA). The counter electrode was a pure lithium metal disc with a diameter of 14.3 mm and a thickness of 75 μm (Alfa Aesar). Li—S cells were assembled using LIR 2032 coin cells inside an Ar-filled glovebox, and the electrolyte volume added in the separator was ≈ 88 μL.

2.3. Electrochemical measurements

The assembled cells were investigated using a multichannel BT2000 Arbin test system (Texas, USA) between 1.7 and 2.7 V vs. Li^+, a voltage range that permitted the observation of characteristic voltage plateaus of Li—S batteries [32,33]. The electrochemical behavior of the S-SiOC cathode was investigated by a galvanostatic charge-discharge (GCD) technique, which has been conducted at different C-rates in the range of 0.05 to 2.0 C (1C = 1675 mA g_s^{-1}). Electrochemical impedance spectra

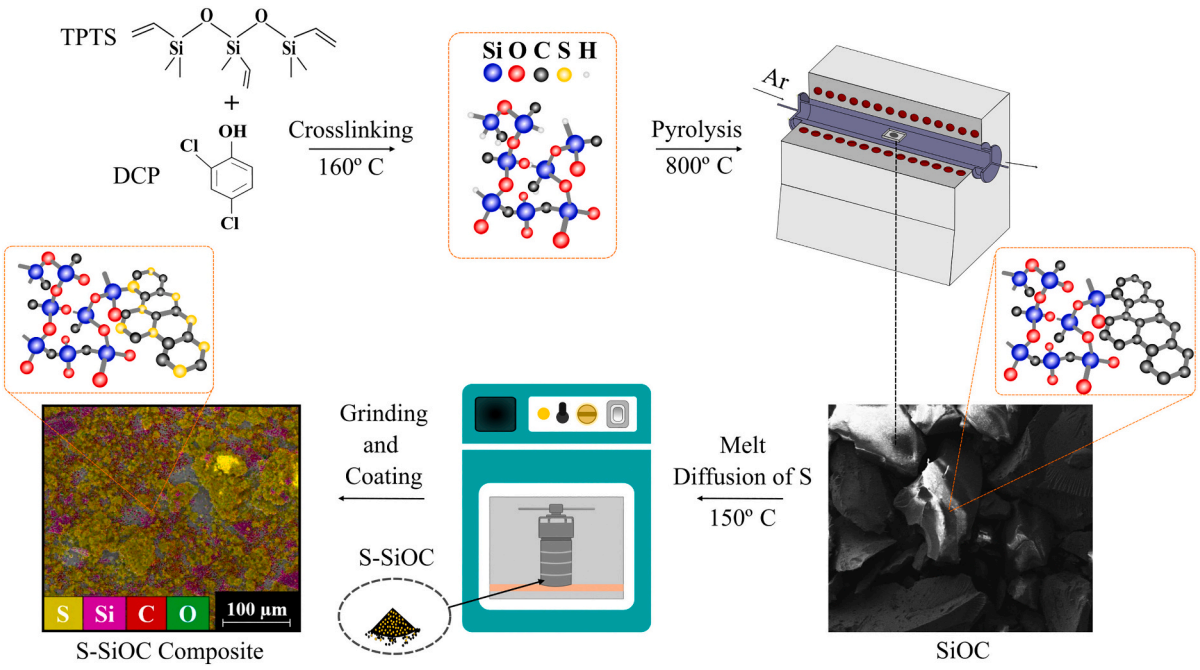

Fig. 1. Fabrication route of the SiOC and S-SiOC powders, depicting the cross-linking, pyrolysis, melt diffusion, grinding, and coating processes.

(EIS) measurements were conducted from 100 mHz to 100 kHz at an AC amplitude of 5 mV using an electrochemical workstation (CH Instruments, USA).

2.4. Materials characterization

The structural changes during the fabrication process of the SiOC and S-SiOC powders was investigated by Fourier transform infrared (FTIR) spectroscopy analysis, which was conducted using an infrared spectrometer model Spectrum 400 (PerkinElmer, Inc.) equipped with a deuterated triglycine sulfate (DTGS) detector for the mid-infrared range. The analysis was conducted in the attenuated total reflectance (ATR) mode using a reflectance accessory model GladiATR (Pike Inc.) comprising a diamond prism, and presenting a spectra resolution of 4 cm^{-1}.

The SSA and the pore volume of the SiOC power were investigated by Brunauer–Emmett–Teller (BET) surface area analyzer, which was determined by N_2 adsorption at 77 K using a Micromeritics 3Flex 5.03 analyzer model. The sulfur melt-diffusion process of the S-SiOC, and the crystallinity of the S-SiOC electrodes have been confirmed by Raman spectroscopy, conducted under the HeNe laser source with a wavelength of 632.8 nm (≈ 1.96 eV), using a confocal micro-Raman microscope model LabRAM ARAMIS (Horiba Jobin Yvon Inc.). Spectra were acquired using five accumulations, an acquisition time of 10 s, and a 10 × lens. Raman spectroscopy has also been conducted under a laser source with a wavelength of 785 nm (≈ 1.58 eV), using a micro-Raman spectrometer model in Renishaw inVia, at room temperature.

Furthermore, the presence of sulfur in the S-SiOC powder was also confirmed by X-ray diffraction (XRD), using PANalytical Empyrean model with 45 kV, 40 mA power setting, and a step size of 0.02° with a scan speed of 1°/min. The composition of the SiOC and S-SiOC powders was also analyzed by X-ray photoelectron spectroscopy (XPS), through a scanning microprobe spectrometer with a beam energy of 1486.7 eV (PHI Quantera SXM). The post-cycled S-SiOC electrode was also analyzed by use of XPS, through a spectrometer with a beam energy of 1486.6 eV (Thermo Scientific Al K-alpha+ XPS/UPS system, USA). The sulfur ratio of the S-SiOC powder was evidenced by thermogravimetric analysis (TGA), conducted using a TG 209 F1 Libra (NETZSCH) system, under N_2 gas flowing, with a flow rate of 50 ml/min, heating rate of 10 °C/min, resolution of 0.1 µg, and temperature range of 22–800 °C.

Scanning electron microscopy was used to study the morphology of the powders using a Carl Zeiss EVO MA10 microscope (New York, USA) with 5–30 kV impinging voltage to characterize powder materials. After the casting process, the morphology of the S-SiOC electrode coated on aluminum foil was studied using an FEI Nova NanoSEM 450 scanning electron microscope (SEM) that was also used to study the S-SiOC elemental mapping analysis via energy dispersive X-ray (EDX) spectroscopy.

2.5. Li_2S_6 solution preparation and UV–vis adsorption test

A visualized adsorption test was conducted by adding SiOC powder in a Li_2S_6 solution, which was further analyzed by ultraviolet-visible (UV–Vis) spectroscopy. The preparation of the Li_2S_6 solution consisted in mixing Li_2S (Sigma Aldrich) and S_8 (Sigma Aldrich) with a stoichiometric ratio of 5:1 in the electrolyte previously detailed, which was stirred and heated at 60 °C for 24 h. To conduct the visualized test, 70 mg of SiOC powder was added to 3 ml of the Li_2S_6 solution. Then, after the adsorption tests, the solutions were placed into a quartz cuvette and were analyzed by UV–Vis spectroscopy using an AGILENT 8453 UV-VIS spectrophotometer model, in absorbance mode, with run interval (λ) of 190 nm to 1100 nm. The radiation source consisted of a combination of two lamps: deuterium and tungsten.

3. Results and discussion

3.1. Morphological and structural analyses of the SiOC and S-SiOC composite powders

The structural changes between the precursor (TPTS) and the PDC electrode (SiOC) obtained after the pyrolysis procedure, and the composite material (S-SiOC) were revealed by FTIR spectroscopy (Fig. S1). The FTIR spectra of the TPTS and the cross-linked TPTS showed several bands that have previously been detailed [25], while the spectrum of the SiOC powder showed bands assigned to Si—O stretching and Si—C stretching vibration bonds, respectively positioned at 1035 and 785 cm^{-1}. These bands were also present after the sulfur loading process, and a decrease in band intensity and a downshift were observed. For

example, Si—O and Si—C bands were positioned at 992 and 759 cm^{-1} (Fig. S1) [34,35], and were of lower intensity likely due to the infrared inactivity of sulfur [36].

However, this study used TPTS-derived SiOC powder instead of the TPTS-derived SiOC fiber that presented a hollow structure, as reported by Mujib et al. [25]. Therefore, nitrogen adsorption-desorption analysis (Fig. S2) was conducted to evaluate the SSA and the pore size distribution of the TPTS-SiOC powder. The high SSA of the SiOC, proved by BET, indicated a value of 235 $m^2\ g^{-1}$, consistent with SiOC materials prepared under similar conditions as reported in the past [37,38].

Furthermore, after the sulfur diffusion into the SiOC structure, Raman spectroscopy was conducted to characterize the carbon vibrational modes of the S-SiOC composite powder. Raman analyses were conducted using laser beams with wavelengths of 632.8 nm (HeNe source) and 785 nm, and both spectra displayed sulfur bands, confirming the melt-diffusion process. However, the HeNe laser source (632.8 nm) caused fluorescence during the analysis, and the Raman spectrum of the SiOC powder (Fig. S3) has not displayed the carbon bands, while the Raman spectrum of the S-SiOC powder inhibited some features of the sulfur bands (Fig. S4). On the other hand, the Raman spectroscopy analyses under the 785 nm laser source (Fig. 2a) clearly evidenced bands corresponding to sulfur [39,40] and carbon [25].

The Raman spectrum of the SiOC (Fig. S5a) and S-SiOC (Fig. S5b) powders, under the laser with the wavelength of 785 nm, efficiently evidenced carbon bands, particularly the D band, assigned to disordered aromatic rings, and the G band, attributed to sp^2-hybridized carbon atoms [41]. Moreover, the deconvolution displayed bands beyond the D and G bands, which consists of the D* band, assigned to disordered graphitic lattices, D″ band, assigned to amorphous phases, and D′ band, which is associated with a single-phonon intravalley scattering process [42]. After the deconvolution process, the Raman spectrum of the SiOC powder presented an I_D/I_G ratio of 1.63 and an $I(A_D)/I(A_G)$ ratio of 4.4 (see Table S1 to observe the peak parameters). The crystallite sizes of the SiOC powder were calculated by Eq. (1), proposed by Cançado et al. [43] (Eq. (1)), and considering the $I(A_D)/I(A_G)$ as conducted by Kaspar et al. [44], indicating that the material has crystallite sizes (L_a) of ≈ 20.5 nm. After the melt-diffusion process, the S-SiOC composite powder presented an I_D/I_G ratio of 1.84 and an $I(A_D)/I(A_G)$ ratio of 4.94 (see Table S2 to observe the peak parameters), which are slightly higher than the results from the SiOC powder, indicating an increase in the disordered structure of the S-SiOC after the melt-diffusion process.

$$L_a(\mathrm{nm}) = \left(2.4 \times 10^{-10}\right)\lambda^4 \left(\frac{I(A_D)}{I(A_G)}\right)^{-1} \quad (1)$$

Furthermore, the presence of sulfur in the S-SiOC composite was also probed by XRD, as the resulting patterns displayed the crystallographic

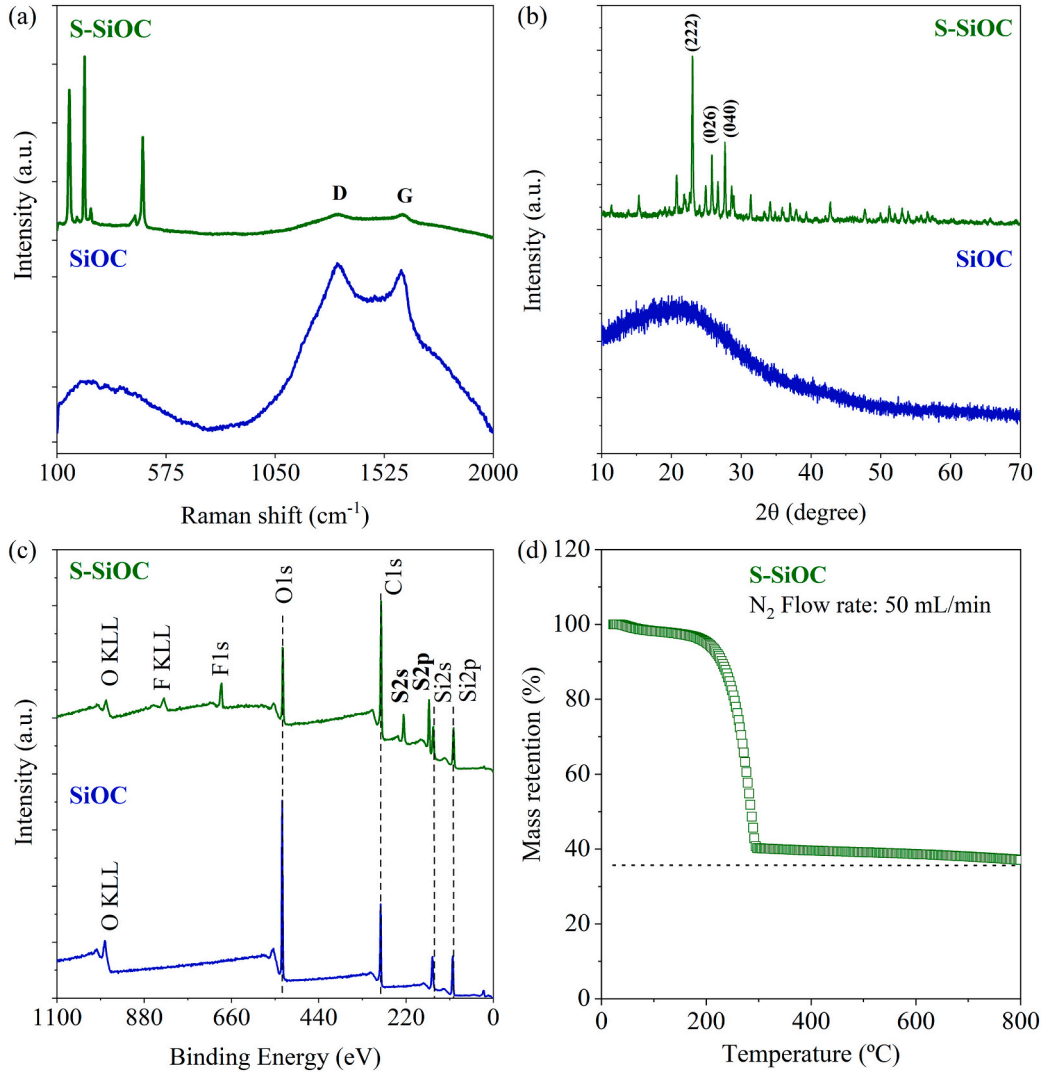

Fig. 2. (a) Raman spectra of the SiOC and S-SiOC powders. Laser wavelength: 785 nm (1.58 eV), Exposure time: 20 s, accumulations: 2, laser power: 5 %, lens: 50 ×. (b) XRD patterns, and (c) XPS survey spectra of the SiOC and S-SiOC powders. (d) TGA of the S-SiOC powder.

structures of the SiOC and the S-SiOC powders, and clearly evidenced peaks attributed to sulfur in the pattern of the S-SiOC powder (Fig. 2b). The XRD pattern of the SiOC powder presented a common result for amorphous materials, displaying a broad peak at 21°, associated with a combination between the silica matrix and carbon [45]. Furthermore, the XRD pattern of the S-SiOC composite presented peaks attributed to sulfur, particularly the ones displayed at 23°, 25.8°, ad 27.7°, which are respectively assigned to the (222), (026), and (040) reflections of sulfur (Fig. 2b) [46].

The presence of sulfur in the composition of the S-SiOC powder was also evidenced by XPS spectroscopy, which can be observed in the XPS survey spectra of the SiOC and S-SiOC powders (Fig. 2c). The survey XPS spectrum of the SiOC powder displayed the C_{1s}, O_{1s}, and Si_{2p} peaks (Fig. 2c), while the survey XPS spectrum of the S-SiOC powder also displayed the presence of the S_{2p} peak. The XPS survey spectrum of the S-SiOC powder also detected a minimal amount of fluorine (F_{1s}) that was assumed to have resulted from the use of a Teflon vessel during the melt-diffusion process. TGA analysis also confirmed the sulfur-loading process in the S-SiOC powder and quantified the amount of sulfur by monitoring the weight loss of the sample during the heating process. The TGA curve showed a mass decrease of 60–65 %, indicating that nearly all the sulfur evaporated from the S-SiOC structure, while part of the sulfur may have bonded to the carbon in the SiOC (Fig. 2d).

SEM was also used to investigate the morphologies of the SiOC powder before the melt-diffusion process (Fig. 3ai), commercial sulfur powder (Fig. 3aii), and S-SiOC composite powder, after the sulfur melt-diffusion process (Fig. 3aiii), evidencing the presence of sulfur in the composite S-SiOC powder. Furthermore, after the electrode coating process, the presence of sulfur in the active S-SiOC electrode on the aluminum foil was confirmed by SEM images under different magnitudes (Fig. 3bi-iii), and the homogenous distribution of sulfur in the S-SiOC structure was proved by EDX elemental mapping, showing the efficiency of the sulfur-melting diffusion procedure (Fig. 3c). The EDX spectrum of the S-SiOC powder (Fig. S6a) also confirmed the presence of sulfur in the S-SiOC electrode. The EDX spectrum also was in accordance with a previous EDX spectrum of TPTS-derived SiOC fiber in a previous study [25], except for the presence of sulfur.

The high-resolution XPS spectra of the SiOC powder, displayed in Fig. S7, details the bonding of the SiOC powder pyrolyzed at 800 °C, and the curve fitting process has been done for the Si_{2p}, C_{1s}, and O_{1s} orbitals. The curve fitting of the Si_{2p} unraveled the presence of $SiCO_3$ (102.5 eV) and SiO_4 (102.4 eV) [47], the C_{1s} peak indicated as the presence of C—Si (283.8 eV), C═C (284.5 eV), and C═O (288 eV), and the O1s peak displayed Si—O (532 eV) and C—O (532.4 eV) bonds, which is in accordance with other SiOC materials previously investigated [25,48].

Furthermore, the high-resolution XPS spectra of the S-SiOC powder evidenced peaks assigned to S_{2p} (Fig. 4a), Si_{2p} (Fig. 4b), C_{1s} (Fig. 4c), and O_{1s} (Fig. 4d) orbitals. The high-resolution XPS spectra of the Si_{2p} (Fig. 4b), C_{1s} (Fig. 4c), and O_{1s} (Fig. 4d) peaks evidenced the same bonds previously observed in the high-resolution XPS spectra of the SiOC powder (Fig. S7). The high-resolution spectrum of the S_{2p} peak (Fig. 4a) confirmed the sulfur loading on the SiOC powder and the efficiency of the melt-diffusion process (Fig. 1). The peaks from the S_{2p} orbital was deconvoluted into $S_{2p3/2}$ and $S_{2p1/2}$ doublets, with an intensity and area ratio of 2:1 ($S_{2p3/2}$:$S_{2p1/2}$), and an energy separation of ≈ 1.2 eV between these bands (see Table S3), which is in accordance with previous results from the literature [49,50]. The deconvolution details the C—S bond, which has been deconvoluted into two bands, particularly the $S_{2p3/2}$ and $S_{2p1/2}$ doublet, respectively positioned at 161.4 eV and 162.6 eV, which is consistent with previous results from the literature [36,51,52]. The

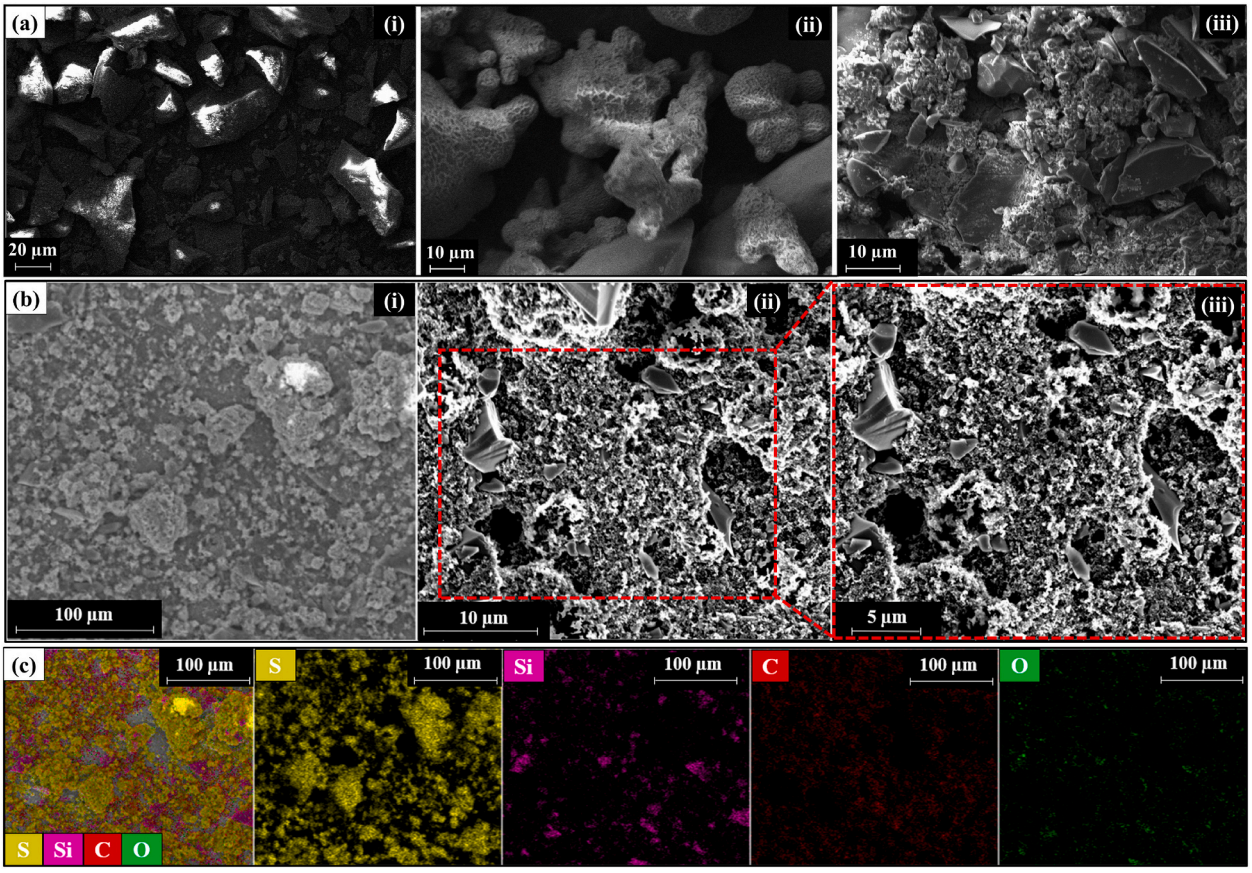

Fig. 3. (a) SEM images of the (i) SiOC powder, (ii) commercial sulfur powder, and (iii) S-SiOC composite powder. (b) SEM images of the S-SiOC electrode coated on aluminum foil under different magnifications, as displayed by the scale bars with (i) 100 µm, (ii) 10 µm, and (iii) 5 µm. (c) Elemental mapping of the S-SiOC composite electrode, confirming the presence of sulfur in the structure of the composite electrode. (d) High-resolution XPS spectra of the S-SiOC composite powder.

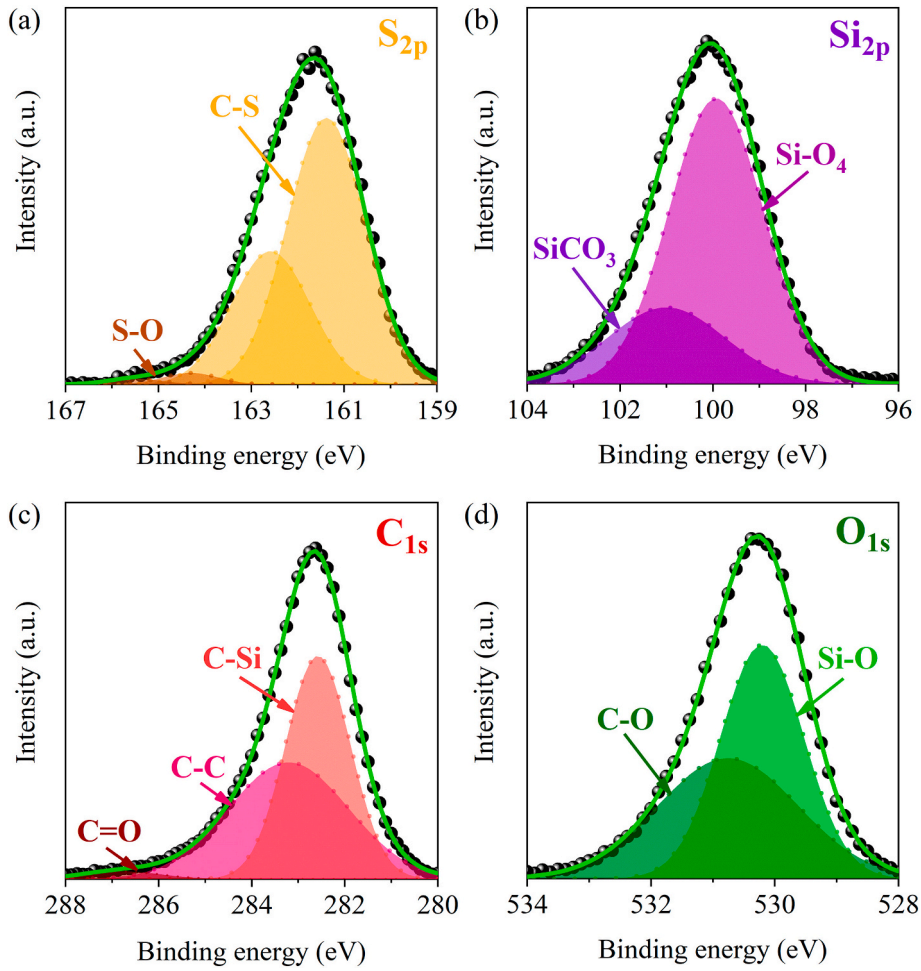

Fig. 4. High-resolution XPS spectra of the S-SiOC powder, displaying the (a) S_{2p}, (b) Si_{2p}, (c) C_{1s}, and (d) O_{1s} orbitals.

S_{2p} high-resolution spectrum also displays bands assigned to oxidized sulfur species [53], positioned at 164.7 eV and 165.5 eV.

3.2. Electrochemical results

A galvanostatic charge-discharge test was performed at a gravimetric current of 83.75 mA g_s^{-1}, i.e., 0.05C (considering 1C = 1675 mA g^{-1}). The electrochemical analyses, displayed in Fig. 5, were normalized by mass of sulfur in the electrode. The initial cycle of the Li—S batteries (Fig. 5a) produced two plateaus, respectively positioned at ≈ 2.32 V and ≈ 2.2 V in the charge and discharge profiles, in accordance with the transition oxidation states of sulfur (Fig. 5a). The first plateau was attributed to the reduction of elemental sulfur (S_8) to high-order LiPS (Li_2S_n, $6 \leq n \leq 8$) as a reaction between the ring-opened sulfur and lithium, while the second plateau was attributed to the reduction of low-order LiPS (Li_2S_n, $2 \leq n \leq 6$). The charging process also showed the same two plateaus (at ≈ 2.21 V and ≈ 2.24 V), in accordance with the transition states [1].

The cyclability test at the C-rate of 0.05C (Fig. 5a and b) followed a current value close to a previous study conducted by Qu et al., which investigated SiCN as a sulfur host for Li—S batteries at a current density of 83.5 mA g^{-1}. The study conducted by Qu et al. investigated SiCN pyrolyzed at different temperatures, including 800 °C [22], same pyrolysis temperature as that used in the present study.

Based on the sulfur content of 56 wt% in the specimen, sulfur areal loading of 0.663 mg cm^{-2} and the first cycle's gravimetric discharge capacity of ≈ 1420 mAh g_s^{-1} at 0.05C, the specific energy and power densities of the Li—S cell with the S-SiOC cathode were found to be 1384 Wh $kg^{-1}$and 81.65 W Kg^{-1}, respectively using Eqs. (S1) and (S2) (see the parameters in Table S4, and the comparison with theoretical Li—S system in Table S5). These values are comparable to previously published works [54,55].

Fig. 5(a) displays the charge-discharge profiles at 0.05C, displaying the 1st, 2nd, 3rd, 10th, and 50th cycles. The voltage-capacity profiles are quite similar during the constant-current charging process, owing to the formation of long-chain LiPS. The discharge curves followed the same pattern, with all profiles exhibiting similar reducing LiPS plateaus. Upon examining the more advanced cycles, it is noted that the difference in the charge capacity between the 10th and 50th cycles is not significant, indicating that the S-SiOC electrode underwent the passivation process and considerable reduction in its cyclability was during the initial cycles, which is expected for Li—S batteries. This phenomenon probably occurs due to the shuttle effect, which reduces the active area of the sulfur electrode [1]. However, the system soon exhibits remarkable stability for the remaining battery cycles, providing a reversible capacity of 711 mAh gs^{-1} after 50 cycles (Fig. 5a and b), still retaining 50.3 % of its initial capacity, which indicates a small capacity loss after the five initial cycles.

However, a fast capacity loss was observed in the initial five cycles, resulting in a charge capacity of 718 mAh g_s^{-1} in the sixth cycle, retaining 50.8 % of the initial capacity. This capacity loss in the initial cycles has been previously reported in the literature, indicating that active sulfur has been consumed in the initial cycles, while the capacity results of the next cycles results have resulted from the conversion reactions of the sulfur present into the porous electrode [56]. Despite the initial cycles, the S-SiOC electrode provided a stable cycling process in

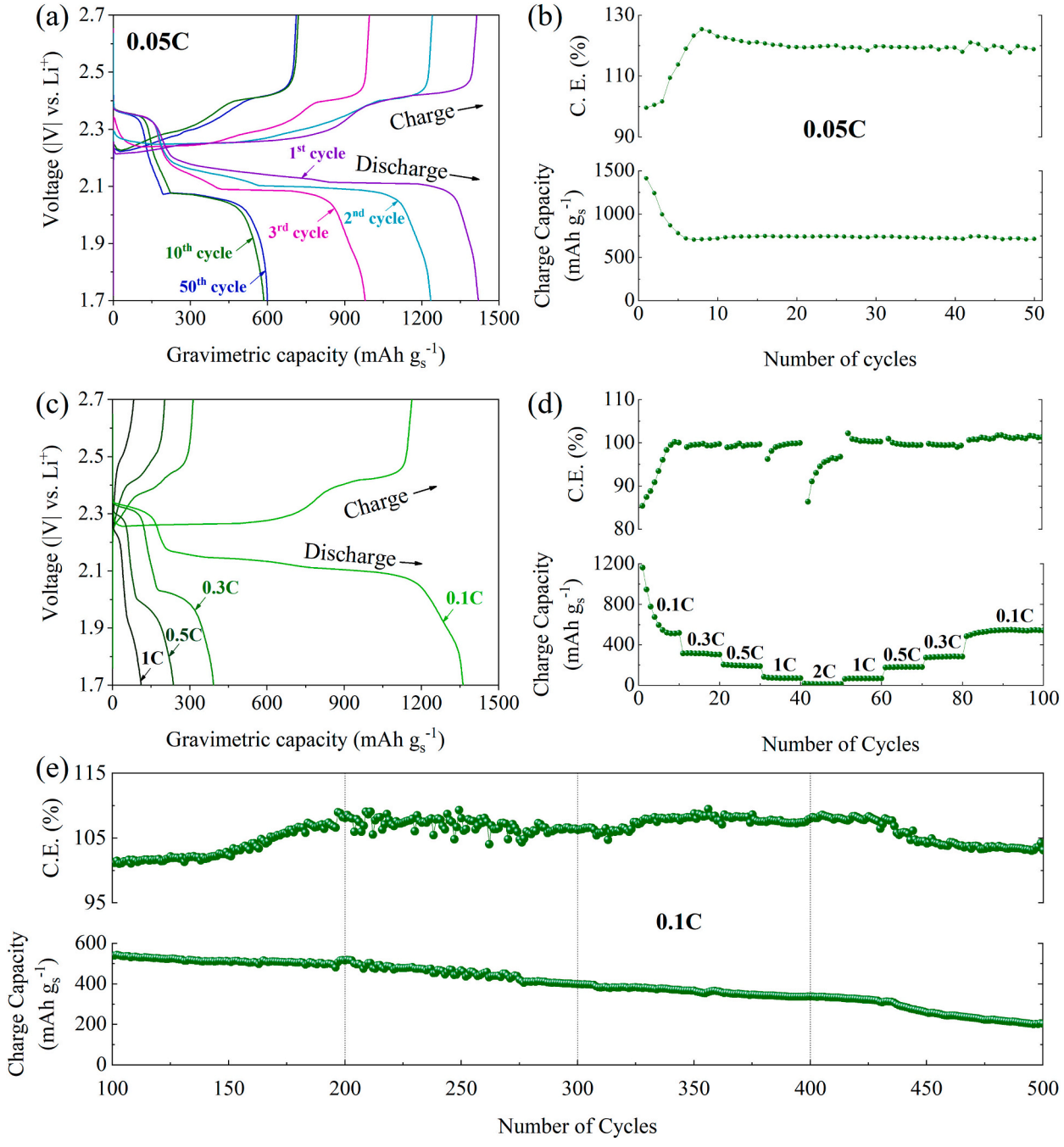

Fig. 5. Charge-Discharge performance of the S-SiOC composite as the cathode of Li—S cells. (a) Voltage profile of the 1st, 2nd, 3rd, 10th, and 50th cycles at 0.05 C, (b) Cycling stability data for 50 cycles at 0.05 C. (c) Voltage profile of the initial cycles at 0.1 C, 0.3 C, 0.5 C, and 1 C. (d) Charge capacity values for 0.1 C, 0.3 C, 0.5 C, 1 C, and 2 C. (e) Cyclability test, which consisted of conducting 400 cycles at 0.1 C after the C-rate test. Electrolyte: 1 M LiTFSI in DOL/DME (v/v, 1:1) containing 1 wt % of $LiNO_3$. 1C = 1675 mA g_s^{-1}

comparison to the SiCN host material pyrolyzed at the same temperature reported elsewhere [22] (see Fig. S8).

During the discharging process, long chains of soluble LiPS pass through the separator, form short chains of LiPS, and reach the lithium anode. During the charging process, these short chains of LiPS migrate back to the cathode and are re-oxidized, forming long chains of LiPS. Then, coulombic efficiency values higher than 100 % have probably resulted from the diffusion of soluble LiPS [22]. The S-SiOC electrode provided an initial coulombic efficiency of ≈ 99.5 %, presenting significantly higher values for the following cycles, reaching the efficiency of ≈ 125.3 % in the 8th cycle. Then, the efficiency was slightly decreased and presented a stable result, reaching the efficiency of ≈ 118.7 % after 50 cycles at 0.05C (Fig. 5b). Therefore, it is possible to conclude that the increase of the coulombic efficiency for the initial cycles is associated with the higher presence of LiPS in the electrolyte, probably culminating from the cathode sulfur loss during the initial cycles (Fig. 5b), resulting in a longer charging process. Otherwise, the next cycles presented a stable coulombic efficiency, which may indicate a reduced presence of LiPS dissolved into the electrolyte, implying that the SiOC host was efficient in adsorbing LiPS.

Furthermore, present study also performed the rate capability test at C-rate values of 0.1C, 0.3C, 0.5C, 1C, and 2C (considering 1C = 1675 mA g_s^{-1}), totaling 10 cycles for each C-rate. The voltage profile of the initial cycles for each C-rate value showed the same plateaus assigned to the

transition states (Fig. 5c), except for the voltage profile for the high C-rate of 2 C, which showed an extremely low capacity and coulombic efficiency. This study also monitored the recovery capacity by reproducing the C-rate test previously detailed but in reverse order (from 2 C to 0.1 C), proving that the capacity was successfully recovered at 0.1 C.

This Li—S system comprising the S-SiOC electrode was investigated at different C-rate values, and they have shown that the S-SiOC is more appropriate for being applied in systems that operate under low current density (e.g., 0.1C; see Fig. 5d). Furthermore, a cyclability test was performed to investigate the reversible capacity of the same cell at the C-rate of 0.1C for the following 400 cycles (Fig. 5e). The initial charge capacity provided by the S-SiOC cathode was 1162 mAh g_s^{-1} at 0.1C, followed by a decrease after the five initial cycles, reaching a charge capacity of 545 mAh g_s^{-1} for the sixth cycle, retaining ≈ 46.7 % of its initial capacity. The coulombic efficiency provided by the S-SiOC cathode during the cycling process at 0.1C presented a stable result until the ≈ 150th cycle, indicating a higher intensity of the shuttle effect, which is in accordance with the capacity decrease. However, the charge capacity was slightly decreased, presenting values higher than 500 mAh g_s^{-1} (at 0.1C) until the 204th cycle. Then, the capacity was continuously decreased, leading to a reversible charge capacity of 398 mAh g_s^{-1} (at 0.1C) in the 300th cycle, retaining ≈ 34.25 % of its initial capacity, and finally presenting a reversible capacity of 203 mAh g_s^{-1} (at 0.1C) after 500 cycles, corresponding to ≈ 17.47 % of its initial capacity (Fig. 5e). These results have also been compared with another Li—S cell comprising an SiOC-free cathode (also identified as *S* electrode), containing only sulfur as its active material, to compare the efficiency of the S-SiOC electrode. However, the SiOC-free electrode presented a lower initial capacity and fast capacity fade, retaining ≈ 33.2 % of its initial capacity in the 200th cycle, and only ≈ 6.3 % of its initial capacity for the 300th cycle (see Fig. S9).

As the S-SiOC cathode provided low-capacity values under high C-rates (e.g., 0.5C, 1C, and 2C), this material is appropriate for applications that require high cyclability (see Fig. 5d and Fig. 5e), as it has demonstrated outstanding performance for long-term cycling applications, which most Li—S batteries have struggled to achieve [2]. Consequently, the S-SiOC composite is a suitable alternative for the development of novel cathodes for Li—S systems due to the long-term cyclability it offers.

EIS analysis has been conducted before the cycling process, using an LIR 2032 coin cell comprising S-SiOC as the cathode, under the same configuration of the cells assembled for the C-rate and cyclability tests (Fig. 5). In the Nyquist plot (Fig. S10), the interception of the semicircle with the real axis is assigned to the equivalent series resistance (R_e), the semicircle is assigned to the charge-transfer resistance (R_{ct}), and the inclined line at low frequency is attributed to the diffusion of electroactive species in the electrode [57]. The equivalent circuit model used to fit the EIS data consisted of the *Randles* circuit [58] with an open Warburg (W_o) representing the diffusion of LiPS and a constant phase element (CPE) assigned to the double-layer capacitance (inset of Fig. S10). The fitting with the *Randles* circuit presented an equivalent series resistance (R_e) of 14 Ω and a charge-transfer resistance (R_{ct}) of 44 Ω (the parameters are displayed in Table S6), which are in accordance with previous EIS results for Li—S batteries available in the literature [23,59].

3.3. Post-cycling analyses of the S-SiOC cathode

Post-cycling analyses were conducted to monitor structural and morphological changes in the S-SiOC cathode after completing 50 cycles at 0.05C (Fig. 5b). The Li—S battery cells were disassembled in a glove box under Ar atmosphere, and repeatedly rinsed with dimethyl carbonate (DMC) to remove surface contaminants, such as the glass fiber separator and its remaining fibers, and then dried overnight at 60 °C inside an Ar-filled glove box.

The sulfur loss was observed via post-cycling analyses of the S-SiOC electrode after 50 cycles at the C-rate of 0.05C. SEM images of the S-SiOC powder showed the morphology of the composite cathode surface without significant changes from the pristine electrode morphology (Fig. 3b), despite some remaining glass fibers on its surface (Fig. 6a). Furthermore, the elemental mapping (Fig. 6b) and the EDX spectrum (Fig. S6b) of the post-cycling electrode indicated a significant decrease of sulfur on the cathode composition. However, the cyclability test at 0.05C (Fig. 5b) showed a significant capacity decrease in the initial cycles, and the capacity results stabilized after the sixth cycle, demonstrating reversible capacity values higher than 700 mAh g_s^{-1}, indicating that the most of the sulfur loss occurred in the initial five cycles.

The results from Raman spectroscopy evidenced a lower intensity of the sulfur bands for both the pristine S-SiOC electrode and the S-SiOC electrode after 50 cycles at the C-rate of 0.05C (Fig. S11) in comparison to the result from the S-SiOC powder (Fig. S4), under the HeNe laser source (632.8 nm), probably because of the addition of PVDF and carbon black during the electrode fabrication. Unlike the spectrum of the S-SiOC powder that presented fluorescence under the HeNe laser source (632.8 nm), the spectrum of the pristine S-SiOC (Fig. S11a) electrode coated on aluminum foil displayed carbon bands, likely due to the added PVDF and carbon black during electrode fabrication. The deconvolution of this spectrum displayed the D and G bands [31,32,60], as well as D*, D′, and D″ bands [42]. The Raman spectrum of the post-cycling S-SiOC electrode (Fig. S11b) also displayed bands assigned to carbon, likewise the pristine S-SiOC electrode (Fig. S11a). This spectrum presented an I_D/I_G ratio of 1.52, while the S-SiOC electrode presented an I_D/I_G ratio of 1.49 (the peak parameters of the deconvolution of the Raman spectra of the pristine and post-cycling S-SiOC electrodes are available in Table S7), which shows a low decrease of the crystallinity, indicating that the amount of defects in the sulfur host has not significantly increased after the conversion reactions. The difference of the I_D/I_G of the S-SiOC electrodes in comparison to the S-SiOC powder are probably because of the addition of PVDF and carbon black during the electrode fabrication.

The elemental composition and chemical bonds of the post-cycling S-SiOC electrode have also been investigated by XPS. The survey XPS spectrum detailed the same peaks as those observed in S-SiOC powder with some changes; a significant increase in the peaks assigned to oxygen (O_{1s}) and fluorine (F_{1s}) in comparison to the XPS results of the S-SiOC powder was observed, probably because of the addition of PVDF duringt fabrication of the electrode, and the appearance of a peak assigned to Li_{1s} (Fig. S12).

The high-resolution XPS spectra of the post-cycled S-SiOC electrode displays the S_{2p} (Fig. 7a), Si_{2p} (Fig. 7b), C_{1s} (Fig. 7c), and O_{1s} (Fig. 7d) orbitals. However, changes were observed, particularly in the S_{2p} orbital, in comparison to the results of the S-SiOC powder (Fig. 4a). As expected, the SiOC host material efficiently adsorbed LiPS, as evidenced by the high-resolution XPS spectrum of the S_{2p}. The high resolution S_{2p} spectrum of the post-cycled S-SiOC electrode (Fig. 7a) was also deconvoluted into $S_{2p3/2}$ and $S_{2p1/2}$ doublets, with an intensity and area ratio of 2:1 ($S_{2p3/2}$:$S_{2p1/2}$), and energy separation of ≈ 1.2 eV between these bands (see Table S3), which is in accordance with previous results from the literature [49,50]. The deconvolution of this peak indicated the presence of Li—S bonds (160.5 and 161.7 eV), C—S bonds (162.1 and 163.3 eV), and S—S bonds (163.5 and 164.7 eV) [61]. The presence of thiosulfate (167.3 and 168.5 eV) and polythionate (169.4 and 170.6 eV) in the post-cycled cathode could be a result of the strong interaction between the oxygen-rich surface of the S-SiOC electrode and the sulfur from the LiPS [62]. The high-resolution S_{2p} spectrum confirmed that the SiOC host material chemically adsorbs LiPS and inhibits the shuttle effect, as previously observed using SiOCN ceramic as the host material for positive electrodes of Li—S batteries reported elsewhere [23]. It was observed a shift of the $SiCO_3$ band in the high-resolution XPS spectrum of the Si_{2p} peak (Fig. 7b), in comparison to the Si_{2p} XPS spectrum of the S-SiOC powder (Fig. 4b). The high-resolution XPS spectrum of the C_{1s} peak (Fig. 7c) revealed an increased intensity of the peak assigned to

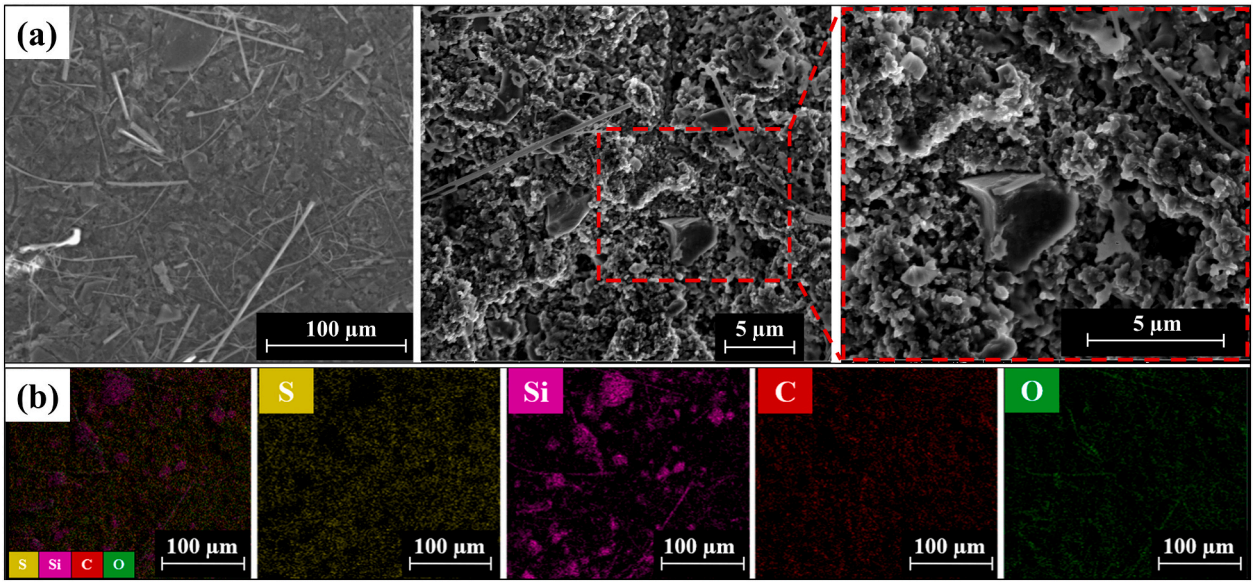

Fig. 6. Post-cycling (a) SEM images and (b) elemental mapping. The analyses were conducted after 50 cycles at 0.05C.

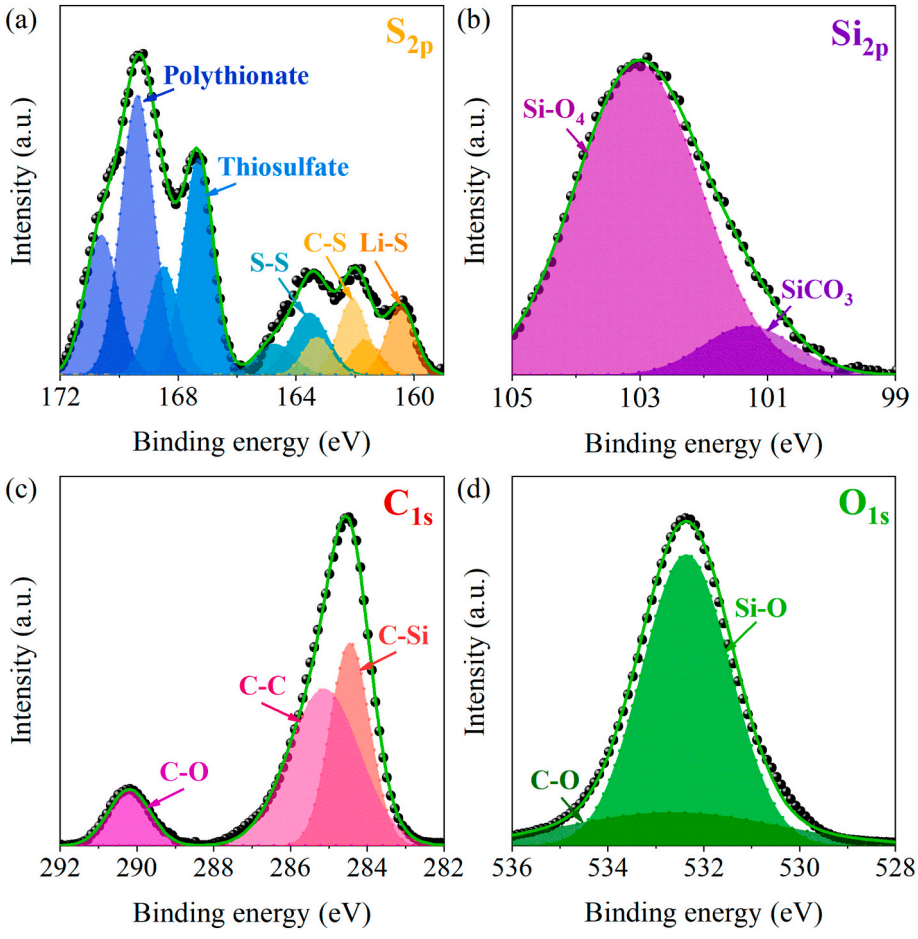

Fig. 7. High-resolution XPS spectra of the post-cycling S-SiOC electrode, displaying the (a) S_{2p}, (b) Si_{2p}, (c) C_{1s}, and (d) O_{1s} peaks.

C—O bond in the post-cycled S-SiOC cathode, which could be associated with the formation of Li_2CO_3, resulting from the interaction between Li^+ ions and the –(CO_3)– groups of the SiOC, or from the formation of the solid-electrolyte interphase (SEI) layer [63].

Furthermore, a visualized adsorption test was conducted to analyze the interaction between the SiOC powder and the LiPS. To conduct this test, a blank Li_2S_6 solution was prepared, which initially presented a yellow color (Fig. 8ai), and after the addition of 70 mg of SiOC powder into 3 ml of the Li_2S_6 solution, it immediately turned black (Fig. 8aii). Then, the solution started to become transparent with time, showing a

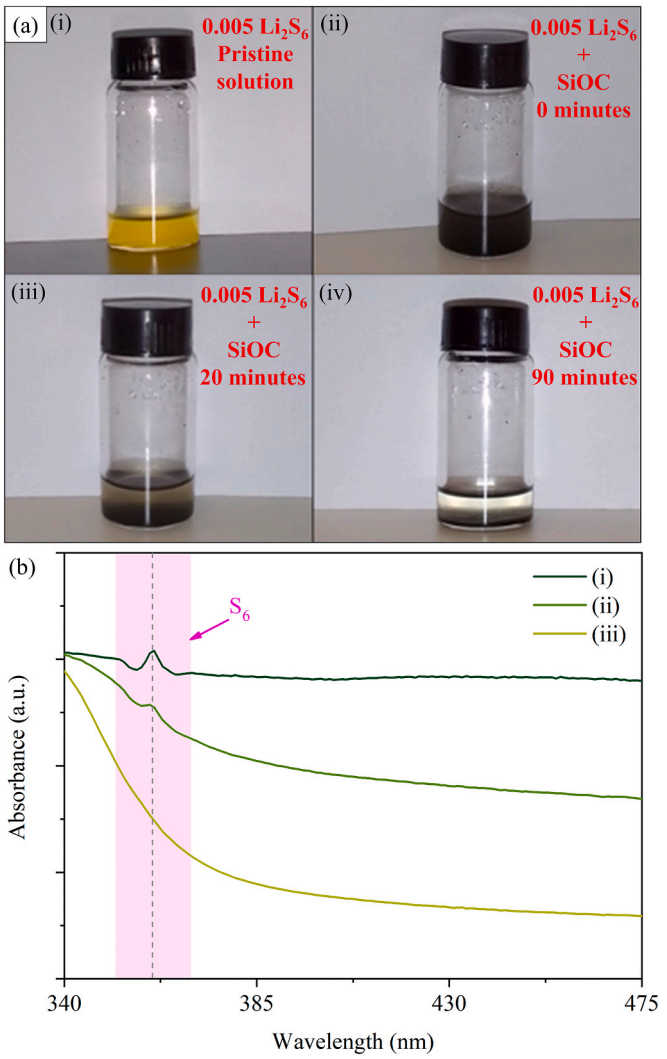

Fig. 8. (a) Digital photographs displaying the (i) Li_2S_6 pristine solution, (ii) immediately after the addition of the SiOC powder, (iii) after 20 min, and (iv) after 90 min. (b) UV–Vis spectrum of (i) 0.005 M Li_2S_6 dissolved into an electrolyte solution (1 LiTFSI +1 % wt. $LiNO_3$ dissolved into DOL:DME – 1:1); (ii) after 20 min, and (iii) after 90 min of the addition of 70 mg of SiOC in the Li_2S_6 solution.

translucent shade after 20 min (Fig. 8aiii) and presenting an almost transparent shade after 90 min (Fig. 8aiv). Furthermore, UV–Vis spectroscopy has also demonstrated the efficiency of the SiOC in adsorbing LiPS. The UV–Vis spectrum of the blank Li_2S_6 solution (Fig. 8bi) displayed a band centered at 361 cm^{-1}, assigned to S_6^{2-}, which has been previously reported in the literature [64,65]. After the addition of SiOC powder, it was observed that the S_6^{2-} band was significantly decreased after 20 min (Fig. 8bii), and fully disappeared after 90 min (Fig. 8biii), confirming the ability of the SiOC in adsorbing LiPS.

Also, FTIR spectroscopy was used to investigate the pristine S-SiOC electrode and the post-cycled S-SiOC electrode, revealing bands assigned to C—H_2 stretching bond [25] at 1326 cm^{-1}, S═O asymmetric and S═O symmetric stretching bonds [66], respectively positioned at 1192 and 1124 cm^{-1}, and Si—O stretching bond [25] at 1003 cm^{-1} (see Fig. S13), which are summarized in Table S8. The results have shown a significant increase in the intensity of the bands assigned to the S═O asymmetric and symmetric stretching bonds, probably due to the adsorption of LiPS by the oxygen-rich S-SiOC electrode, as suggested by the XPS results.

4. Conclusion

In summary, SiOC powder synthesized via a polymer pyrolysis process was used to fabricate a novel sulfur melt-infiltrated SiOC composite as stable cathode material for Li—S batteries. The morphology and structure of the S-SiOC powder and the S-SiOC electrode were investigated by the use of microscopic and spectroscopic techniques confirming the successful loading of sulfur (≈ 70 wt%) in the SiOC host material. The electrochemical analysis indicated that the S-SiOC composite electrode efficiently adsorbed LiPS and exhibited a stable performance after some capacity loss in the initial five cycles. A charge capacity of 711 mAh g_s^{-1} after 50 cycles at 0.05C, retaining ≈ 50.3 % of its initial capacity was observed, which is considerably higher than other PDCs sulfur host materials for cathodes of Li—S batteries. Results from a test conducted at a C-rate of 0.1C revealed a reversible charge capacity of 398 mAh g_s^{-1} after 300 cycles (≈ 34.25 % of its initial capacity) and 203 mAh g_s^{-1} after 500 cycles (≈ 17.47 % of its initial capacity). Therefore, this study demonstrates that polymer-derived SiOC ceramics should be further investigated as a sulfur host material for Li—S batteries because of the significant capacity retention, mainly under low C-rates (e.g., 0.05C and 0.1C).

CRediT authorship contribution statement

Murilo M. Amaral: Writing – original draft, Methodology, Investigation, Data curation, Conceptualization. **Shakir Bin Mujib:** Writing – review & editing, Methodology, Investigation, Validation. **Erick A. Santos:** Writing – review & editing, Investigation, Validation. **Josimar Ribeiro:** Writing – review & editing. **Hudson Zanin:** Supervision, Project administration, Funding acquisition. **Gurpreet Singh:** Writing – review & editing, Methodology, Conceptualization, Resources, Supervision, Project administration, Funding acquisition.

Declaration of competing interest

The authors declare that they have no known competing financial interests or personal relationships that could have appeared to influence the work reported in this paper.

Data availability

Data will be made available on request.

Acknowledgment

M. M. Amaral, S. B. Mujib, and G. Singh would like to acknowledge Kansas State University for providing financial support. They also are grateful for the National Science Foundation Grant (Award Number: 1743701) and CMMI NSF CAREER Grant (Award Number 1454151). M. M. Amaral, E. A. Santos, and H. Zanin are grateful for the financial support received from Unicamp Development Foundation – FUNCAMP and the São Paulo Research Foundation – FAPESP (2021/09387-1; 2022/02222-0). The research was performed in part in the Nebraska Nanoscale Facility: National Nanotechnology Coordinated Infrastructure and the Nebraska Center for Materials and Nanoscience (and/or NERCF), which are supported by the National Science Foundation under Award ECCS: 2025298, and the Nebraska Research Initiative. The research was also conducted in part at the Institute for Bioengineering Research (University of Kansas), at the Nanoscale Characterization and Fabrication Laboratory (Virginia Tech University), and at the University of Illinois, Urbana-Champaign. The authors gratefully acknowledge the Brazilian Center for Research in Energy and Materials (CNPEM), particularly the Brazilian Synchrotron Light Laboratory (LNLS).

Appendix A. Supplementary data

Supplementary data to this article can be found online at https://doi.org/10.1016/j.est.2023.108388.

References

[1] A. Manthiram, Y. Fu, S.-H. Chung, C. Zu, Y.-S. Su, Chem. Rev. 114 (2014) 11751–11787.
[2] J.B. Robinson, K. Xi, R.V. Kumar, A.C. Ferrari, H. Au, M.-M. Titirici, A. Parra-Puerto, A. Kucernak, S.D.S. Fitch, N. Garcia-Araez, Z.L. Brown, M. Pasta, L. Furness, A.J. Kibler, D.A. Walsh, L.R. Johnson, C. Holc, G.N. Newton, N. R. Champness, F. Markoulidis, C. Crean, R.C.T. Slade, E.I. Andritsos, Q. Cai, S. Babar, T. Zhang, C. Lekakou, N. Kulkarni, A.J.E. Rettie, R. Jervis, M. Cornish, M. Marinescu, G. Offer, Z. Li, L. Bird, C.P. Grey, M. Chhowalla, D. Di Lecce, R. E. Owen, T.S. Miller, D.J.L. Brett, S. Liatard, D. Ainsworth, P.R. Shearing, J. Phys. Energy 3 (2021) 031501.
[3] C. Yang, P. Li, J. Yu, L.-D. Zhao, L. Kong, Energy 201 (2020), 117718.
[4] H. Danuta, U. Juliusz, Electric Dry Cells and Storage Batteries, 3,043,896, 1962.
[5] J. Liang, Z.-H. Sun, F. Li, H.-M. Cheng, Energy Storage Mater. 2 (2016) 76–106.
[6] X. Ji, K.T. Lee, L.F. Nazar, Nat. Mater. 8 (2009) 500–506.
[7] A. Abdul Razzaq, Y. Yao, R. Shah, P. Qi, L. Miao, M. Chen, X. Zhao, Y. Peng, Z. Deng, Energy Storage Mater. 16 (2019) 194–202.
[8] T. Yang, J. Xia, Z. Piao, L. Yang, S. Zhang, Y. Xing, G. Zhou, ACS Nano 15 (2021) 13901–13923.
[9] L. Ji, M. Rao, H. Zheng, L. Zhang, Y. Li, W. Duan, J. Guo, E.J. Cairns, Y. Zhang, J. Am. Chem. Soc. 133 (2011) 18522–18525.
[10] H. Chen, P. Xia, W. Lei, Y. Pan, Y. Zou, Z. Ma, J. Porous. Mater. 26 (2019) 1325–1333.
[11] G. Zheng, Q. Zhang, J.J. Cha, Y. Yang, W. Li, Z.W. Seh, Y. Cui, Nano Lett. 13 (2013) 1265–1270.
[12] X. Tao, J. Wang, C. Liu, H. Wang, H. Yao, G. Zheng, Z.W. Seh, Q. Cai, W. Li, G. Zhou, C. Zu, Y. Cui, Nat. Commun. 7 (2016) 11203.
[13] J. He, Y. Chen, A. Manthiram, Energy Environ. Sci. 11 (2018) 2560–2568.
[14] G. Cui, G. Li, D. Luo, Y. Zhang, Y. Zhao, D. Wang, J. Wang, Z. Zhang, X. Wang, Z. Chen, Nano Energy 72 (2020), 104685.
[15] J. Zhou, S. Li, X. Ji, W. Sun, Y. Yang, Chem. Eng. J. 382 (2020), 122843.
[16] T. Liu, H. Hu, X. Ding, H. Yuan, C. Jin, J. Nai, Y. Liu, Y. Wang, Y. Wan, X. Tao, Energy Storage Mater 30 (2020) 346–366.
[17] P. Colombo, G. Mera, R. Riedel, G.D. Sorarù, J. Am. Ceram. Soc. 93 (2010) 1805–1837.
[18] S. Bin Mujib, G. Singh, Int J. Ceram, Eng. Sci. 4 (2022) 4–9.
[19] S. Mukherjee, Z. Ren, G. Singh, J. Phys. D. Appl. Phys. 51 (2018), 463001.
[20] Q. Wen, F. Qu, Z. Yu, M. Graczyk-Zajac, X. Xiong, R. Riedel, J. Adv. Ceram. 11 (2022) 197–246.
[21] F. Qu, M. Graczyk-Zajac, D. Vrankovic, N. Chai, Z. Yu, R. Riedel, Electrochim. Acta 384 (2021), 138265.
[22] F. Qu, Z. Yu, M. Krol, N. Chai, R. Riedel, M. Graczyk-Zajac, Nanomaterials 12 (2022) 1283.
[23] J. Lu, J. Hu, H. Zhong, Y. Ren, L. Zhang, J. Alloys Compd. 860 (2021), 157903.
[24] M. Weinberger, J. Munding, M. Lindén, M. Wohlfahrt-Mehrens, Energy Technol. 6 (2018) 1797–1804.
[25] S. Bin Mujib, F. Ribot, C. Gervais, G. Singh, RSC Adv. 11 (2021) 35440–35454.
[26] L. Wang, Z.-Y. Wang, J.-F. Wu, G.-R. Li, S. Liu, X.-P. Gao, Nano Energy 77 (2020), 105173.
[27] M. Zhong, J. Guan, J. Sun, X. Shu, H. Ding, L. Chen, N. Zhou, Z. Xiao, Energy Storage Mater 41 (2021) 588–598.
[28] Z. Xu, J. Wang, J. Yang, X. Miao, R. Chen, J. Qian, R. Miao, Angew. Chem. 128 (2016) 10528–10531.
[29] Z. Wang, B. Wang, Y. Yang, Y. Cui, Z. Wang, B. Chen, G. Qian, ACS Appl. Mater. Interfaces 7 (2015) 20999–21004.
[30] F. Liu, Q. Xiao, H. Bin Wu, L. Shen, D. Xu, M. Cai, Y. Lu, Adv. Energy Mater. 8 (2018) 1701744.
[31] X. Li, J. Liang, W. Li, J. Luo, X. Li, X. Yang, Y. Hu, Q. Xiao, W. Zhang, R. Li, T.-K. Sham, X. Sun, Chem. Mater. 31 (2019) 2002–2009.
[32] J. Xu, D. Su, W. Zhang, W. Bao, G. Wang, J. Mater. Chem. A Mater. 4 (2016) 17381–17393.
[33] H. Kim, J. Lee, H. Ahn, O. Kim, M.J. Park, Nat. Commun. 6 (2015) 7278.
[34] G. Socrates, Infrared and Raman Characteristic Group Frequencies, 3rd ed., John Wiley & Sons, Ltd, 2004, pp. 241–246.
[35] M. Naviroj, S.M. Miller, P. Colombo, K.T. Faber, J. Eur. Ceram. Soc. 35 (2015) 2225–2232.
[36] Z. Wang, Y. Dong, H. Li, Z. Zhao, H. Bin Wu, C. Hao, S. Liu, J. Qiu, X.W. Lou, Nat. Commun. 5 (2014) 5002.
[37] S. Bin Mujib, R. Cuccato, S. Mukherjee, G. Franchin, P. Colombo, G. Singh, Ceram. Int. 46 (2020) 3565–3573.
[38] V.S. Pradeep, D.G. Ayana, M. Graczyk-Zajac, G.D. Soraru, R. Riedel, Electrochim. Acta 157 (2015) 41–45.
[39] A. Anderson, Y.T. Loh, Can. J. Chem. 47 (1969) 879–884.
[40] A.T. Ward, J. Phys. Chem. 72 (1968) 4133–4139.
[41] B. Dong, Y. Han, T. Wang, Z. Lei, Y. Chen, F. Wang, H. Abadikhah, S.A. Khan, L. Hao, X. Xu, R. Cao, L. Yin, S. Agathopoulos, ACS Appl. Energy Mater. 3 (2020) 10183–10191.
[42] D. López-Díaz, M. López Holgado, J.L. García-Fierro, M.M. Velázquez, J. Phys. Chem. C 121 (2017) 20489–20497.
[43] L.G. Cançado, K. Takai, T. Enoki, M. Endo, Y.A. Kim, H. Mizusaki, A. Jorio, L. N. Coelho, R. Magalhães-Paniago, M.A. Pimenta, Appl. Phys. Lett. 88 (2006), 163106.
[44] J. Kaspar, M. Graczyk-Zajac, R. Riedel, J. Power Sources 244 (2013) 450–455.
[45] H. Shi, A. Yuan, J. Xu, J. Power Sources 364 (2017) 288–298.
[46] W. Mao, C. Ma, P. Ni, M. Li, Y. Ding, S. Zhang, J. Pan, F. Cao, K. Bao, ChemElectroChem 7 (2020) 1733–1738.
[47] L. David, R. Bhandavat, U. Barrera, G. Singh, Nat. Commun. 7 (2016) 10998.
[48] Z. Ren, C. Gervais, G. Singh, RSC Adv. 10 (2020) 38446–38455.
[49] L. Ma, H.L. Zhuang, S. Wei, K.E. Hendrickson, M.S. Kim, G. Cohn, R.G. Hennig, L. A. Archer, ACS Nano 10 (2016) 1050–1059.
[50] X. Liang, C. Hart, Q. Pang, A. Garsuch, T. Weiss, L.F. Nazar, Nat. Commun. 6 (2015) 5682.
[51] L. Zhang, L. Ji, P.-A. Glans, Y. Zhang, J. Zhu, J. Guo, Phys. Chem. Chem. Phys. 14 (2012) 13670.
[52] Q. Hu, M.C. Paau, Y. Zhang, X. Gong, L. Zhang, D. Lu, Y. Liu, Q. Liu, J. Yao, M.M. F. Choi, RSC Adv. 4 (2014) 18065–18073.
[53] L. Qie, W. Chen, X. Xiong, C. Hu, F. Zou, P. Hu, Y. Huang, Adv. Sci. 2 (2015) 1500195.
[54] Z. Li, J.T. Zhang, Y.M. Chen, J. Li, X.W. Lou, Nat. Commun. 6 (2015) 8850.
[55] Y. Yang, M.T. McDowell, A. Jackson, J.J. Cha, S.S. Hong, Y. Cui, Nano Lett. 10 (2010) 1486–1491.
[56] G. Tan, R. Xu, Z. Xing, Y. Yuan, J. Lu, J. Wen, C. Liu, L. Ma, C. Zhan, Q. Liu, T. Wu, Z. Jian, R. Shahbazian-Yassar, Y. Ren, D.J. Miller, L.A. Curtiss, X. Ji, K. Amine, Nat. Energy 2 (2017) 17090.
[57] M. Wang, H. Zhang, Y. Zhang, J. Li, F. Zhang, W. Hu, J. Solid State Electrochem. 17 (2013) 2243–2250.
[58] A. Lasia, in: Electrochemical Impedance Spectroscopy and its Applications, Springer New York, New York, NY, 2014, pp. 85–125.
[59] Á. Doñoro, Á. Muñoz-Mauricio, V. Etacheri, Batteries 7 (2021) 26.
[60] M.S. Dresselhaus, A. Jorio, R. Saito, Annu. Rev. Condens. Matter. Phys. 1 (2010) 89–108.
[61] C. Zhang, Y. Lin, J. Liu, J. Mater. Chem. A Mater. 3 (2015) 10760–10766.
[62] B. Lee, T. Kang, H. Lee, J.S. Samdani, Y. Jung, C. Zhang, Z. Yu, G. Xu, L. Cheng, S. Byun, Y.M. Lee, K. Amine, J. Yu, Adv. Energy Mater. 10 (2020) 1903934.
[63] P.M. Shanthi, P.J. Hanumantha, B. Gattu, M. Sweeney, M.K. Datta, P.N. Kumta, Electrochim. Acta 229 (2017) 208–218.
[64] Z. Liu, H. Qiu, L. Weng, M. Luo, X. Wang, Q. Wang, D. Zhang, Ionics (Kiel) 28 (2022) 5351–5359.
[65] Q. Zou, Y.-C. Lu, J. Phys. Chem. Lett. 7 (2016) 1518–1525.
[66] Y. Diao, K. Xie, S. Xiong, X. Hong, J. Electrochem. Soc. 159 (2012) A1816–A1821.